Biogeosciences

Open Access

EGU

Limits and CO$_2$ equilibration of near-coast alkalinity enhancement

Jing He[1,★] **and Michael D. Tyka**[2,★]

[1]MIT-WHOI Joint Program in Oceanography and Applied Ocean Science and Engineering, Cambridge, MA, 02139, USA
[2]Google Inc., 601 N 34th St, Seattle, WA 98103, USA
★These authors contributed equally to this work.

Correspondence: Michael D. Tyka (mike.tyka@gmail.com)

Abstract. Ocean alkalinity enhancement (OAE) has recently gained attention as a potential method for carbon dioxide removal (CDR) at gigatonne (Gt) scale, with near-coast OAE operations being economically favorable due to proximity to mineral and energy sources. In this paper we study critical questions which determine the scale and viability of OAE. Which coastal locations are able to sustain a large flux of alkalinity at minimal pH and Ω_{Arag} (aragonite saturation) changes? What is the interference distance between adjacent OAE projects? How much CO$_2$ is absorbed per unit of alkalinity added? How quickly does the induced CO$_2$ deficiency equilibrate with the atmosphere? Choosing relatively conservative constraints on ΔpH or ΔOmega, we examine the limits of OAE using the ECCO LLC270 (0.3°) global circulation model. We find that the sustainable OAE rate varies over 1–2 orders of magnitude between different coasts and exhibits complex patterns and non-local dependencies which vary from region to region. In general, OAE in areas of strong coastal currents enables the largest fluxes and depending on the direction of these currents, neighboring OAE sites can exhibit dependencies as far as 400 km or more. At these steady state fluxes most regional stretches of coastline are able to accommodate on the order of 10s to 100s of megatonnes of negative emissions within 300 km of the coast. We conclude that near-coastal OAE has the potential to scale globally to several Gt CO$_2$ yr^{-1} of drawdown with conservative pH constraints, if the effort is spread over the majority of available coastlines. Depending on the location, we find a diverse set of equilibration kinetics, determined by the interplay of gas exchange and surface residence time. Most locations reach an uptake efficiency plateau of 0.6–0.8 mol CO$_2$ per mol of alkalinity after 3–4 years, after which there is only slow additional CO$_2$ uptake. Regions of significant downwelling (e.g.,

around Iceland) should be avoided by OAE deployments, as in such locations up to half of the CDR potential of OAE can be lost to bottom waters. The most ideal locations, reaching a molar uptake ratio of around 0.8, include North Madagascar, California, Brazil, Peru and locations close to the Southern Ocean such as Tasmania, Kerguelen and Patagonia, where the gas exchange appears to occur faster than the surface residence time. However, some locations (e.g., Hawaii) take significantly longer to equilibrate (up to 8–10 years) but can still eventually achieve high uptake ratios.

1 Introduction

To mitigate the worst effects of climate change, the Paris Agreement aims to limit global temperature warming to below 2 °C. This requires not only rapid decarbonization, but also negative CO$_2$ emission technologies (NET) (Rogelj et al., 2018). About 150–800 GtCO$_2$ of net negative emissions are needed in the IPCC SSP1-1.9–SSP1-2.6 scenarios (in addition to decarbonization) to limit global warming to 2 °C by 2100, and this scenario further assumes net negative annual emissions towards the end of the century (Rogelj et al., 2018; IPCC, 2005, 2021).

On geological time scales the Earth regulates atmospheric CO$_2$ concentrations by the combined action of surface rock weathering and ocean CO$_2$ uptake (Penman et al., 2020). High CO$_2$ conditions lead to elevated temperatures and an intensified hydrological cycle, which increases silicate rock weathering (Archer et al., 2009). The subsequently dissolved alkalinity increases the ocean's capacity for CO$_2$ and the excess atmospheric CO$_2$ dissolves into the ocean, largely reacting to form (bi)carbonate ions (Zeebe and Wolf-Gladrow,

2001). Indeed the ocean's total dissolved inorganic carbon (DIC) exceeds that of the current atmosphere by 50-fold (Sarmiento and Gruber, 2006).

This mechanism operates on a 10–100 ka time scale (Archer et al., 2009), limited by the slow intrinsic kinetics of silicate rock dissolution and the slow introduction of un-weathered rock. Exposure of fresh igneous rocks has been linked to rapid cooling of the Earth's past climate (Gernon et al., 2021). Unfortunately, this natural homeostat operates too slowly to mitigate anthropogenic climate change this century. Ocean alkalinity enhancement (OAE) (Renforth and Henderson, 2017) is a proposed approach to accelerate this process in order to increase the ocean's capacity for CO_2 and draw down some of the anthropogenic atmospheric CO_2.

The kinetics of rock dissolution can be accelerated in a number of ways. The simplest approach is to increase the rock's surface area through grinding. Powdered rocks such as olivine can then be added to the ocean and will dissolve over the course of years to decades, adding alkalinity (Hangx and Spiers, 2009; Schuiling and de Boer, 2011; Renforth, 2012; Montserrat et al., 2017; Rigopoulos et al., 2018; Meysman and Montserrat, 2017). Alternatively, some rocks (e.g., $CaCO_3$) may be preprocessed by calcining, transforming them into more rapidly dissolving substances, such as CaO (Kheshgi, 1995). Major concerns with these approaches are the risk of $CaCO_3$ precipitation (Moras et al., 2022; Hartmann et al., 2022), which would remove alkalinity from the ocean, and the introduction of co-contaminants into the ocean. Iron, abundant in most olivine minerals, could inadvertently fertilize the ocean and cause significant ecological effects (Bach et al., 2019). Silicates would likely shift the phytoplankton species composition towards diatoms (Bach et al., 2019). The impact of heavy metals, such as nickel (Guo et al., 2022) is likely complex (Ferderer et al., 2022) and species-specific. Finally, changes in turbidity and large energy costs of grinding (Li and Hitch, 2015) make deployment of particles $< 10 \, \mu m$ impractical, while deployment of coarser particles is limited to shallow waters, as the dissolution is much slower (Montserrat et al., 2017). The long dissolution times also delay the beneficial effects on atmospheric CO_2 concentrations, likely by decades.

An alternative to direct addition of rock mass to the ocean are electrochemical methods which effectively remove acidity from seawater and neutralize it using rocks on land. Acid could be neutralized by using mine tailings and other industrial wastes or by pumping it into underground basalt formations (Matter et al., 2009; McGrail et al., 2006; Goldberg et al., 2008). Several variants has been proposed based on electrolysis (House et al., 2007; Rau, 2009; Davies et al., 2018) or bipolar electrodialysis (Eisaman et al., 2018; de Lannoy et al., 2018; Digdaya et al., 2020), all essentially producing either pure NaOH or a basified seawater stream, which would be returned to the ocean to increase the pH and elicit CO_2 drawdown. The disadvantage is the significant electrical energy requirement and the fact that the produced

alkalinity is relatively dilute ($\sim 1 \, mol \, kg^{-1}$; de Lannoy et al., 2018), exacerbating transport costs out to sea compared to shipping powdered rock. Prior assessments of shipping costs (Renforth, 2012) when using dedicated fleets have focused on transport of rock-based solid alkalinity (notably olivine), which has a high molality of alkalinity ($\sim 25 \, mol \, kg^{-1}$).

Regardless of the alkalinity source, OAE methods leverage the marine carbonate system (Renforth and Henderson, 2017), a multiple equilibrium state (Zeebe and Wolf-Gladrow, 2001) described by the reaction

$$CO_{2(atm)} \rightleftharpoons CO_{2(aq)} + H_2O \rightleftharpoons H^+ + HCO_3^-$$
$$\rightleftharpoons 2H^+ + CO_3^{2-}. \tag{R1}$$
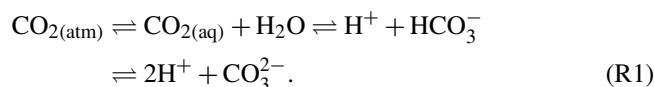
Dissolved inorganic carbon (DIC) is the combined concentration of all carbonate species. Addition of alkalinity (e.g., OH^-) shifts the above equilibrium to the right by consuming H^+ ions, thus lowering the partial pressure of CO_2 in the ocean and driving further ocean CO_2 uptake (Middelburg et al., 2020; Zeebe and Wolf-Gladrow, 2001). As the sea-surface CO_2 exchange is rate limiting (surface water experiences an equilibration time scale on the order of weeks to years; Jones et al., 2014), the addition of alkalinity causes a local increase in pH and aragonite saturation (Ω_{Arag}) and a decrease in pCO_2, all of which could potentially affect the local ecology (Subhas et al., 2022; Ferderer et al., 2022; Bach et al., 2019). Furthermore, increases in aragonite saturation could lead to precipitation of calcium carbonate, which removes alkalinity from the surface water and is counterproductive with respect to CO_2 uptake (Moras et al., 2022; Hartmann et al., 2022). A number of previous studies have used ocean circulation models combined with a carbon cycle model to estimate the carbon uptake potential of various hypothetical OAE scenarios (Köhler et al., 2013; González and Ilyina, 2016; Feng et al., 2017; Ilyina et al., 2013; Keller et al., 2014; Burt et al., 2021; Tyka et al., 2022). Some of these studies investigated very high rates of alkalinity injection to test the limits of OAE. Ilyina et al. (2013) simulated alkalinity addition on the order of $2.8 \, P \, mol \, yr^{-1}$ (for an approximate uptake of $50 \, Gt \, CO_2 \, yr^{-1}$). González and Ilyina (2016) added enough alkalinity to remove around $44 \, Gt \, CO_2 \, yr^{-1}$. Both these studies found drastic changes in pH and the carbonate saturation state.

Most of these simulations consider globally uniform alkalinity injection patterns, which is unrealistic for practical deployment and provides little insight into which geographical locations are ideal for conducting OAE. An ideal region (for purposes of negative emissions) minimizes the effect of added alkalinity on the local carbonate system and ecology, while maximizing the CO_2 uptake per unit alkalinity added.

Several authors have conducted scenario-driven and locally resolved simulations. Köhler et al. (2013) investigated finely ground olivine addition from ship tracks for a total uptake of $3.2 \, Gt \, CO_2 \, yr^{-1}$, simulating the distribution of alkalinity via ballast water of commercial ships. These ship

tracks span the full ocean extent from $40° \text{S}$ to $60° \text{N}$, although heavily weighted to the area between $20°$ and $50° \text{N}$.

Feng et al. (2017) simulated adding olivine along global coastlines where continental shelves are shallower than 200 m. They found that to stay below aragonite saturation levels of $\Omega_{\text{Arag}} = 3.4$ and $\Omega_{\text{Arag}} = 9$, coastal olivine addition can remove around 12 and $36 \, \text{Gt} \, CO_2 \, \text{yr}^{-1}$, respectively. Some more spatially resolved studies have been undertaken. Burt et al. (2021) tested regional alkalinity addition based on eight hydrodynamic regimes in a $1.5°$ model, and Tyka et al. (2022) simulated alkalinity addition at individual points in a $6°$ lat-long grid. Both studies revealed that the pH sensitivity and the efficiency of CO_2 uptake vary geographically and temporally.

Here, we also study alkalinity addition through a practical and economic lens, focusing on electrochemical methods, which produce NaOH or other rapidly dissolving forms of alkalinity. We begin with the assumption that the optimal places for electrochemical alkalinity production would be on the coast, with access both to seawater and low-cost renewable electricity. To minimize risks to coastal ecosystems and ensure adequate spreading and quick dilution, the alkalinity would be transported some distance offshore. This is increasingly critical for larger scale deployments to avoid high concentrations of alkalinity. We wish to determine how far offshore and over what area alkalinity can be added to the surface ocean while staying within conservative biological and geochemical limits. While these issues are less relevant to initial small-scale OAE, our goal is to examine the limits of the technology's potential scale. A judicious amount of OAE may also be beneficial by stabilizing or reversing the anthropogenic acidification of the surface ocean (Albright et al., 2016; Feng et al., 2016). Specific implementations of OAE may also be subject to additional limitations such as trace metal contamination (Guo et al., 2022; Bach et al., 2019), which we do not address here.

Increases in alkalinity change the activities of all forms of CO_2 in the carbonate system (Middelburg et al., 2020; Zeebe and Wolf-Gladrow, 2001), many of which are relevant to marine organisms (Riebesell and Tortell, 2011). Both the direct impact on marine species and the risk of triggering calcium carbonate precipitation must be considered (Bach et al., 2019; Hartmann et al., 2022). Given the complexity of the carbonate system and the variety of responses to each parameter there is no single "correct" choice of proxy (Fassbender et al., 2021) by which to quantify the shift in carbonate state, although the parameters are strongly correlated with each other. Furthermore, what constitutes a safe limit for any given ocean parameter is under debate and likely varies significantly between regions; thus, a blanket hard limit is difficult to establish. Here we use two proxies to quantify changes in the carbonate system: ΔpH and $\Delta\Omega_{\text{Arag}}$.

Prior studies simulated the addition of uniform amounts of alkalinity over some defined area and measured the varying response of ocean parameters. However, because the sensitivity of these parameters varies over more than one order of magnitude, we designed our experiment in reverse, i.e., we adjust the alkalinity addition rate in each grid cell to result in a uniform and relatively small change of a given parameter. We can then examine how the injection rate varies and construct maps that indicate regions of high suitability for OAE.

Finally, to assess the effectiveness and time scale of CO_2 uptake due to an OAE deployment in a given region of interest, we can define the uptake efficiency η_{CO_2} as

$$\eta_{CO_2}(t) = \frac{\Delta\text{DIC}(t)}{\Delta\text{Alk}}, \tag{1}$$

where t denotes the time since alkalinity was added and η_{CO_2} is a unitless molar ratio. Following the addition of some quantity ΔAlk to seawater, the ocean will begin taking up CO_2, eventually reaching a maximum $\eta_{CO_2}(t = \infty) \approx 0.8$ (Renforth and Henderson, 2017; Tyka et al., 2022). The exact value depends on the parameters of the carbonate system, i.e., Alk, DIC, temperature etc., with a typical range of 0.75–0.85 (Tyka et al., 2022). However, the kinetics of this equilibration are known to vary spatially due to differences in the gas exchange time scales and the surface residence time of CO_2-deficient water (Jones et al., 2014; Burt et al., 2021). We thus conducted simulated experiments with short localized pulse injections, followed by tracking of the total excess alkalinity and DIC relative to a reference simulation as done previously with a much coarser model (Tyka et al., 2022). This gives an accurate picture of where alkalinity from a particular injection point is advected to, how much alkalinity is lost to the deep ocean, and how much and when CO_2 uptake can be expected.

2 Methods

2.1 The model

We use the ECCO LLC270 physical fields (Zhang et al., 2018) to simulate the transport of alkalinity by currents and model alkalinity addition in near-coast areas globally. We inject alkalinity to the simulation in strips along all global coastlines, 37 km wide and larger. The ECCO is an ocean state estimate based on the MIT General Circulation Model (MITgcm) (Marshall et al., 1997) that also integrates all available ocean data since the onset of satellite altimetry in 1992. The ECCO uses the adjoint method to iteratively adjust the initial conditions, boundary conditions, forcing fields, and mixing parameters to minimize the model-data errors (Wunsch et al., 2009; Wunsch and Heimbach, 2013). This produces a three-dimensional continuous ocean state estimate that agrees well with observational data. We use the LLC270 configuration with a $1/3°$ horizontal resolution (Zhang et al., 2018). All input and forcing files needed to reproduce the ECCO state estimates and the source code are freely available online, and we use them to reproduce

the LLC270 flow fields. The LLC270 configuration uses a lat-long-cap (LLC) horizontal grid, which uses five faces to cover the globe. The horizontal resolution ranges from 7.3 km at high latitudes to 36.6 km at low latitudes, and has 50 vertical layers with the grid thickness ranging from 10 m near the ocean surface to 458 m at the bottom (Zhang et al., 2018). We use the iteration-42 state estimate described in Carroll et al. (2020), which spans the years 1992–2017.

To represent the ocean carbonate system we used the `gchem` and `DIC` packages within MITgcm. The ocean carbon model was based on Dutkiewicz et al. (2005) and uses five biogeochemical tracers (DIC, alkalinity, phosphate, dissolved organic phosphorus, and oxygen) to simulate the carbonate system. In this model, DIC is advected and mixed by the physical flow fields from the MITgcm, and the sources and sinks of DIC are: CO_2 flux between the ocean and atmosphere, freshwater flux, biological production, and the formation of calcium carbonate shells. The biogeochemical tracers were initialized with contemporary data from GLO-DAPv2 mapped climatologies (Lauvset et al., 2016; Olsen et al., 2017) where possible, or using data from Dutkiewicz et al. (2005) and were allowed to relax locally by running 100 years of forward simulation (looping the ECCO forcing fields). Atmospheric CO_2 concentrations were held constant at 415 µatm, rather than trying to anticipate future emission scenarios. The surface carbonate tracers were found to stabilize during this time.

As we are not simulating a full Earth system, our model does not account for feedbacks of other carbon sinks which reduce the impact of moving CO_2 from the atmosphere to the ocean (Keller et al., 2018). Wind speeds, used to calculate the gas exchange, are imported from the LLC270 forcing data and the air-sea exchange of CO_2 is parameterized with a uniform gas transfer coefficient (Wanninkhof, 1992). To simulate ocean OAE, we forced the simulation by adding pure alkalinity to the surface ocean in specified locations to the top grid cell (10 m depth) and at a parameterized rate; this assumes that alkalinity is of an effectively instantly dissolving nature, such as an NaOH solution. This avoids complicating factors arising from slower dissolving materials such as fine olivine powder, for which dissolution rates vary with ocean conditions and may sink out of the surface layers before complete dissolution (Fakhraee et al., 2022). We focused on alkalinity addition in coastal bands following shorelines because that is economically most viable and accessible for shipping or pipelines. Feedbacks of elevated alkalinity on the rate of surface calcification are also not explicitly modeled.

Six coastal strips are examined with widths of approximately 37, 74, 111, 185, 296 and 592 km, although they vary slightly due to the varying grid cell sizes in the LLC270 grid. Feng et al. (2017) used a coarser 3.6° longitude by 1.8° latitude model, and their injection pattern roughly corresponds to our 296 km coastal strip. The much finer LLC model allows us to resolve coastal features in greater detail and to test thinner injection strips. We also examined injection in discrete locations spaced 200 or 400 km apart along the coastline, in circular patches ≈ 120 km wide.

All runs presented in this paper use the same approach: First a reference simulation is run (spanning 20 ECCO years 1994–2014). Then a second run is conducted with the same starting conditions, with an alkalinity forcing added, which perturbs the system in some way. We then analyze the difference in the carbonate systems (ΔpH, $\Delta\Omega$, ΔDIC, etc.) between these two runs. As the carbonate model does not influence the flow field, there is no divergence in the flow fields over the 20 simulation years and the 2 trajectories are directly comparable. These simulations are run on a small MPI cluster (13 machines, 59 processes each) on Google Cloud Engine, and take about 6 h of wall time per simulation year.

2.2 pH and Omega limits

The carbonate chemistry in different regions varies in its sensitivity to alkalinity injection, owing to local differences in ocean circulation, gas exchange and carbonate chemistry. The goal of our experiments is to determine the maximal alkalinity addition rate which can be sustained at any given grid point and limits the change in one of two surface parameters, pH and the aragonite saturation Ω_{Arag} to some chosen value.

Here we chose target constraints ΔpH$_{tgt} = 0.1$ or $\Delta\Omega_{tgt} = 0.5$. These values are somewhat arbitrary and serve simply to calculate the relative sensitivity of different regions. However, as an intuitive point of reference, the already incurred anthropogenic surface acidification since preindustrial times (Doney et al., 2009) is ΔpH≈ -0.1. Likewise a change of $\Delta\Omega_{Arag} = +0.5$ is unlikely to trigger carbonate precipitation according to Moras et al. (2022) who established an Ω_{Arag} threshold of 5.

An alternative approach would have been to set absolute thresholds for pH and/or Omega; however, we did not pursue this for the following reasons. For the estimation of biological impact a relative change to current conditions seems most appropriate as the local ecosystem is adapted to the local conditions and many biologically relevant stressors change proportionally to the relative concentration change. For example, the energy expenditure of an organism to maintain its intracellular pH is approximately proportional to the logarithm of the proton concentration difference. For purposes of estimating the precipitation limit an absolute threshold would indeed be more appropriate. However, in polar latitudes where Ω_{Arag} is currently low, the change in alkalinity required to reach the limit (e.g., $\Omega_{Arag} > 5$, Moras et al., 2022) would be so large that it would no longer represent a realistic scenario, easily exceed the above relative pH limits and likely exceed the bounds of the simulation's predictive domain. We note that our choice of a relative Omega constraint means that we obtain a lower bound on the true OAE limit, with respect to Omega.

In practice, which limits are acceptable is subject to debate and likely different in different locations. We do not attempt

to anticipate the acceptable limits here, focusing merely on the relative capacity of different ocean regions with respect to these ocean parameters. Our approach is as follows: each surface grid point that is part of the coastal injection strip is given a particular baseline injection rate r (in $mol\,m^{-2}\,s^{-1}$). At every time step and for every grid point, the local (in time and space) ΔpH is calculated using the carbonate model and a reference value obtained from an unperturbed reference simulation ($\Delta pH = pH - pH_{ref}$). If this value is lower than ΔpH_{tgt}, then alkalinity is added according to the baseline rate. If not, then addition is skipped for this time step.

This mechanism is insufficient to ensure the pH does not exceed the maximal value, as the change in pH is determined not only by the local alkalinity addition, but also by advection of alkalinity from neighboring cells and seasonally varying biological activity. We thus iteratively adjusted the baseline rate for each grid cell to empirically determine a rate which gives rise to approximately the desired ΔpH in the following way.

First a pilot simulation was run where the baseline rate was set uniformly to an extreme value of $r = 400\,mol\,m^{-2}\,yr^{-1}$, (higher than any region can accommodate). We ran this simulation for 3 years and recorded the observed amount of addition at each grid cell (generally much lower than the baseline as the above algorithm prevents excessive addition). Second, we reran the simulation using a new, position-dependent baseline rate calculated from the amounts actually added from the pilot simulation using a linear extrapolation to our desired pH maximum. We ran this second simulation for 8 years. We found that the observed ΔpH was now generally very close to the desired ΔpH_{tgt}. However, some regions still exceeded the target value while others undershot. We thus performed a third simulation where we adjusted the addition rate at any grid point inversely proportional to the observed pH deviation, yielding a final third simulation which was allowed to run for 20 years using the ECCO forcing fields from 1995 to 2014. We found that this procedure yielded a relatively narrow distribution of ΔpH or $\Delta\Omega_{Arag}$ for all grid points in the injection strip, although some variability remained (Fig. S1 in the Supplement). A separate iterative optimization was performed for every injection pattern. Grid points outside of the injection strip showed much smaller changes in pH and never exceeded the target ΔpH. The same procedure was used in a separate set of experiments for $\Delta\Omega_{Arag}$.

Once the rate of OAE is stable and acceptable, we can measure how much alkalinity is being added at each grid point. Note that because of the considerable interdependence between nearby grid points there is no one unique injection pattern that satisfies the ΔpH or $\Delta\Omega_{Arag}$ condition; however, multiple independent optimization runs started at different ECCO years yield injection patterns that match very closely.

2.3 Pulse additions

When alkalinity is added to the surface ocean it lowers the partial pressure of CO_2 (pCO_2) and thus increases the rate at which CO_2 dissolves in the ocean surface. The effectiveness η_{CO_2} of this uptake is determined by a number of factors which vary significantly by location. The time scale of gas exchange τ_{CO_2} is approximately 3–9 months and varies by location (Jones et al., 2014), while the residence time τ_{res} of water parcels in the mixed layer varies over shorter times between 2 and 20 weeks.

Thus the resultant equilibration efficiency ratio τ_{res}/τ_{CO_2} was found to be significantly below 1.0 in 95 % of ocean locations (Jones et al., 2014). However, CO_2-deficient water parcels initially lost from the mixed layer can remix into the mixed layer at some later time and thus drive further equilibration elsewhere and over longer time scales. This longer term effect was not explicitly modeled in previous work (Jones et al., 2014) and results in a complex equilibration curve which is not well captured by a single exponential function. As the kinetics of this longer term equilibration depend on the deep transport and mixing of the lost alkalinity, it has to be simulated explicitly.

We extend the work of Jones et al. (2014) by simulating pulse injections of alkalinity in a variety of locations using the ECCO flow fields. These simulations explicitly include all the relevant aspects together (gas exchange, Revelle factor, surface transport, mixed layer-depth, residence time and remixing), by measuring the actual excess CO_2 uptake of the ocean relative to the unperturbed reference simulation. However, because the alkalinity is also distributed horizontally over great distances and mixes from different origins, it is impossible to disambiguate the CO_2 uptake time scale of different injection points from a single simulation. One solution to this problem is to use a Lagrangian approach (van Sebille et al., 2018) which allows the tracking of stochastic particles. Here we chose a simpler approach. For a select number of coastal locations we run a separate simulation and inject a 1-month pulse of alkalinity. Following the pulse we monitor the total excess DIC in the ocean relative to a reference simulation, the distribution of alkalinity across the depth layers, and the pCO_2 deficit at the surface over time. Ideally the length of the pulse would be a single time step; however, this would either necessitate an extreme addition rate or a tiny total quantity of added alkalinity, which would lead to a poor signal to noise ratio during analysis. The choice of pulse length thus represents a compromise, as this length is still much shorter than the overall relaxation time. Ideally such a pulse injection experiment could be conducted for every grid point (as was done with a coarse model in Tyka et al., 2022) and at different times of the year. However, because each pulse requires a whole separate simulation, this exceeded our computation capacity with the high-resolution ECCO model. Thus we chose 17 individual locations of in-

terest along most major coastlines with pulses occurring in January.

2.4　Alkalinity injection from ships

In addition to the steady-state perturbation of ocean parameters over large areas of OAE deployment, it is critical to examine the short-term impacts that arise right at the injection site, which will temporarily take the local carbonate system into an extremely alkaline regime. This is unlikely to be a concern for gradually dissolving alkalinity such as ground olivine (Hangx and Spiers, 2009; Schuiling and de Boer, 2011), but highly relevant for rapidly dissolving alkalinity such as NaOH solution or other solubilized alkaline media.

Of interest is the dilution speed of the added alkalinity (we assume here a solution of 1 M NaOH) against the time scale at which homogeneous nucleation of aragonite is triggered and needs to be avoided. The most natural approach, used also in waste disposal, would be to inject directly into the turbulent wake of the ship to mix the discharge with seawater as rapidly as possible (Renforth and Henderson, 2017). The dilution kinetics have been studied and modeled in previous work (Chou, 1996; IMCO, 1975) and large discrepancies exist between the published models. The IMCO model uses the following empirical form for the unitless dilution factor as function of time t:

$$D(t) = \frac{c}{Q} U^{1.4} L^{1.6} t^{0.4}, \tag{2}$$

where t is time (seconds), Q is the release rate ($\mathrm{m^3\,s^{-1}}$), U is the speed of the ship ($\mathrm{m\,s^{-1}}$), and L is the waterline length (m). C is an empirical constant, set to 0.003 for release from a single orifice and 0.0045 for release from multiple ones. Intuitively, larger speeds and longer ships have more turbulent wakes, producing faster dilution. Chou (1996) used the following similar model which instead of waterline length uses the width of the ship, B, in units of meters, to account for the ship size.

$$D(t) = \frac{0.2108}{Q} U^{1.552} B^{1.448} t^{0.552}. \tag{3}$$

Chou's formula gives much faster dilution rates and was verified against field testing data. Other work (Lewis, 1985; Byrne et al., 1988; Lewis and Riddle, 1989) used even higher exponents on the time t so we take the IMCO formula to be an upper limit although in general no universally applicable law can be expected as the dispersion time scale will inevitably depend on local conditions. For a given starting concentration C_0 of the alkaline effluent (e.g., $1\,\mathrm{mol\,L^{-1}}$ NaOH) we can calculate the resultant alkalinity by considering the dilution with seawater with alkalinity $\mathrm{Alk_0}$

$$\mathrm{Alk}(t) = \frac{1}{D(t)} C_0 + \left(1 - \frac{1}{D(t)}\right) \mathrm{Alk_0}. \tag{4}$$

We can then determine the $\mathrm{pH}(t)$ and the carbonate saturation state $\Omega(t)$ by solving the carbonate system at any given $\mathrm{Alk}(t)$. We used PyCO2SYS (Humphreys et al., 2020) to solve the carbonate system numerically, assuming PyCO2SYS default values and $\mathrm{Alk_0} = 2300\,\mu\mathrm{mol\,kg^{-1}}$ and $\mathrm{DIC} = 2050\,\mu\mathrm{mol\,kg^{-1}}$. These analytical models are valid only on time scales smaller than 1 h, after which dilution kinetics are driven by the local background turbulence rather than the immediate influence of the wake turbulence. Thus longer scale dilution effects will vary substantially from location to location. As the time scale considered here is much shorter than the typical CO_2 gas exchange time scale, we do not explicitly model CO_2 uptake during this initial dilution.

2.5　Estimation of transport costs

Alkalinity prepared on land must be transported out to sea, which adds to the total cost of the achieved negative emissions (in USD per tonne CO_2). While at very small scale it could be released right at the coast, for larger overall OAE deployment the alkalinity will need to be spread over greater areas (to avoid excessive local pH or Omega changes) which increases the cost for every additional unit of alkalinity added. Having obtained maps of the allowable rate of OAE in any given area, we can estimate the transport costs for each of our simulated scenarios. Large-scale maritime shipping costs are currently around USD 0.0016–0.004 per tonne per kilometer (Renforth, 2012). For each grid point where alkalinity is injected, we calculate the distance D to the nearest coast, and take double that to be the minimum round trip distance for a ship to travel. Realistically, a ship will have to travel farther than D since it needs to go to the nearest port or NaOH factory, so this is the lower bound on the transport distance. This allows us to calculate the lower bound of the shipping cost per t CO_2 for each grid point. The scenario model provides the alkalinity injection rate for each grid point, and assuming an eventual uptake efficiency $\Delta_{CO_2} \approx 0.8$ we can obtain the total shipping cost for every grid point. Summing the total cost over all grid points in which injection occurs and dividing by the total expected global CO_2 uptake yields a lower bound of the average effective global transport cost per tonne CO_2.

3　Results and discussion

3.1　Injection capacity

In all our simulations the alkalinity flux in the injection grid cells was iteratively adjusted to elicit a change in pH or the change in Omega (although not simultaneously) to a value of either $\Delta\mathrm{pH} = +0.1$ or $\Delta\Omega_{\mathrm{Arag}} = +0.5$, respectively. Due to the correlation between neighboring grid cells, seasonal and year-to-year changes in currents and biotic activity, these constraints are not perfectly satisfied but we were able to confine them to a narrow range around the desired value (Fig. S1). The injection rate as well as $\Delta\mathrm{pH}$ and $\Delta\Omega_{\mathrm{Arag}}$, stabilize within the first 5–6 years of the simulation and re-

main stable for the remainder of the simulation (Fig. S1), indicating that a steady state is reached where the alkalinity addition rate is matched by outflowing alkalinity into open ocean areas and by neutralization by atmospheric CO_2. Note that while the time-averaged ΔpH is close to 0.1, there is significant temporal variability that leads to ΔpH slightly exceeding 0.1 at some parts of the year (Fig. S1).

As expected, ΔpH or $\Delta\Omega_{Arag}$ outside the injection grid cells is much lower and never exceeds the target value. However, the effect on adjacent areas outside of the injection grid points is variable and depends on the pattern of ocean currents that sweep alkalinity away from injection areas. For instance, western boundary currents carry the coastal excess alkalinity far out into the open ocean, so we see elevated changes in the North Atlantic and Indian oceans, even outside the injection areas.

For each injection pattern and chosen limit we can now obtain a global map of steady-state alkalinity flux (mol m^{-2} yr^{-1}), which shows the variability of capacity for OAE (Fig. 1b, c and d). We note substantial variability on multiple scales. Firstly on a large scale, some coastal areas have a fundamentally greater capacity for distributing and neutralizing alkalinity flux than others (see also Fig. 2b). Large capacities are found around islands which sit in or near ocean currents, as those rapidly sweep the alkalinity away from near-coast areas. Examples include Kerguelen, Easter Island and Hawaii. Continental coasts which exhibit large capacities are found around South and East Africa, off the coast of Peru and Brazil, Southeast Australia and the west coast of Japan. Finally, an area of very large tolerance for alkalinity addition is found in the northern Atlantic. However, as will be shown later, this is due to downwelling and deep water formation, which is highly undesirable for OAE as the alkalinity cannot efficiently equilibrate with the atmosphere before being lost. Conversely inland seas and partially enclosed seas exhibit the smallest capacity for OAE, notably the Red Sea, the Mediterranean and the Baltic Sea. An interesting counterexample is the Gulf of Mexico and the Caribbean Sea which, owing to the traversing Gulf Stream, have significant capacity for OAE. We found no correlation between background pH and OAE rate, as the influence of local ventilation due to currents dominates the capacity for alkalinity addition.

As expected, the large scale patterns obtained by limiting ΔpH $= 0.1$ or $\Delta\Omega_{Arag} = 0.5$ are very similar (Fig. S2) up to a linear factor and highly correlated on a per grid cell basis. This is consistent with the observation that OAE capacity is primarily influenced by local currents. However, we note that the fundamental sensitivities of pH and Ω_{Arag} with respect to Alk change quite differently from the Poles to the Equator. In particular, ∂pH$/\partial$Alk decreases from $\sim 2.6 \times 10^3$ L mol^{-1} at the poles to $\sim 1.0 \times 10^3$ L mol^{-1} at the Equator, while $\partial\Omega/\partial$Alk increases from $\sim 7.6 \times 10^3$ L mol^{-1} at the Poles to $\sim 11 \times 10^3$ L mol^{-1} at the Equator (computed from GLODAPv2, Lauvset et al., 2016; Olsen et al., 2017 data and

pyCO2SYS; Humphreys et al., 2020; Lewis and Wallace, 1998). Furthermore, from the perspective of preventing precipitation due to excessive Ω_{Arag}, the available headroom is much smaller at tropical latitudes, where Ω_{Arag} is already close to 4, than near the poles where Ω_{Arag} is as low as 1–2 (Lauvset et al., 2016; Olsen et al., 2017). Thus, as our relative $\Delta\Omega_{Arag}$ limit was set to 0.5, the OAE limits obtained here should be considered a lower bound with respect to calcite precipitation, i.e., polar regions could tolerate a much larger addition rate. For pH the actual ecologically tolerable limits will vary from coast to coast, and we do not attempt to anticipate them here. We note, however, that for our examined constraints (both of which are very conservative) a significant amount of negative emissions can be obtained even in very narrow coastal strips as the transport out to open sea is very efficient. This observation is consistent with prior work by Feng et al. (2017).

On a fine scale we find that the sustainable injection flux varies over 2–3 orders of magnitude between nearby grid points (Fig. S1) with a distribution that is approximately lognormal. The variance is even larger for thin injection strips (Fig. S1) and very large fluxes can be sustained in some locations if the net transport of alkalinity out of the strip is high enough. Depending on the prevailing currents, the highest injection rate can be found both on the outside and inside of the injection strip.

For all regions we observed that while widening the injection strip increases the total allowable rate of alkalinity injection, the increase is sublinear (Fig. 2a). Every additional unit of alkalinity added needs to be transported further offshore and the average injection rate decreases per unit area. This is consistent with the view that the majority of the neutralization of the added alkalinity by invading CO_2 occurs outside the injection strip and the local pH is primarily determined by the rate of transport of alkalinity into other areas (Burt et al., 2021). This is confirmed by integrating the total CO_2 flux over the injection strip and over the rest of the ocean surface, relative to the reference simulation. Figure 2a shows that especially for thin coastal injection strips, direct gas exchange through the strip surface accounts for only a minor component of the induced CO_2 uptake and the majority occurs outside of the injection areas. As the strip widens, however, this fraction significantly increases. Especially in regions with weak transport we observe that often a larger quantity of alkalinity can be added right at the border of the strip than in the middle, as alkalinity can dilute to bordering areas that are not directly receiving alkalinity (Fig. 3). Indeed, the largest alkalinity fluxes observed occur when the strip widths are very thin (Fig. S1). The consequence is that any particular coastal region can increase its capacity for injection by going further out to sea, but that there are diminishing returns of doing so, i.e., the increase in capacity is sublinear with width.

The influence of widening the injection area is also shown in detail for three regions in Fig. 3 and a larger number of
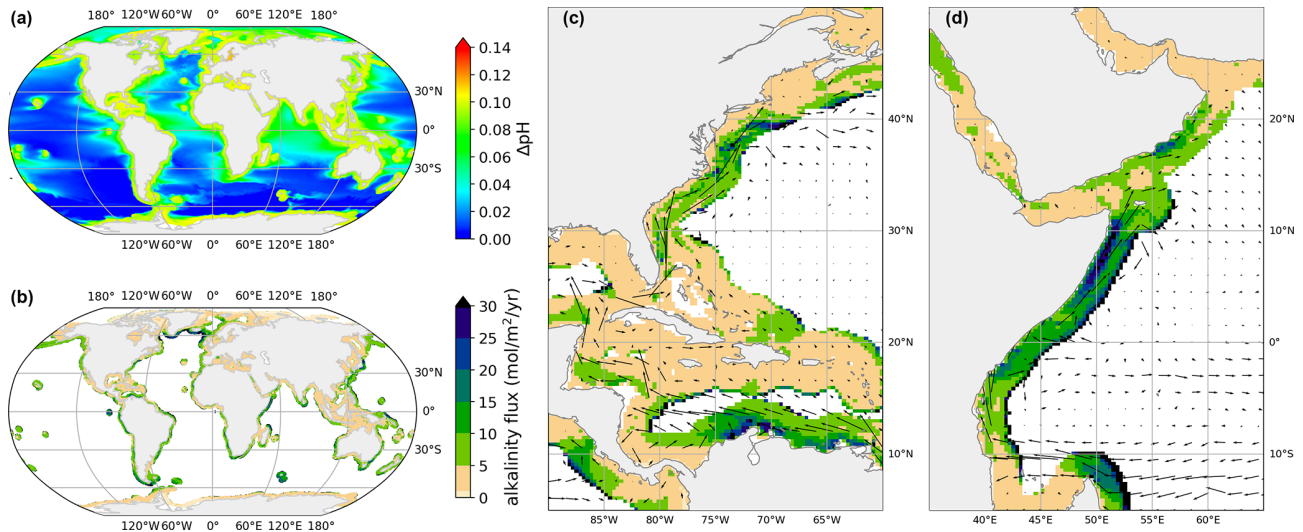
Figure 1. Shown is a coastal injection in a strip 296 km wide, subject to $\Delta pH_{tgt} = 0.1$. All time-averages ran over 5–20 years. **(a)** Averaged pH change compared to a reference simulation with no added alkalinity. **(b)** Average alkalinity flux at each grid point from the coast. **(c, d)** Injection flux for two example regions. Annually averaged surface currents are overlaid as a vector field.
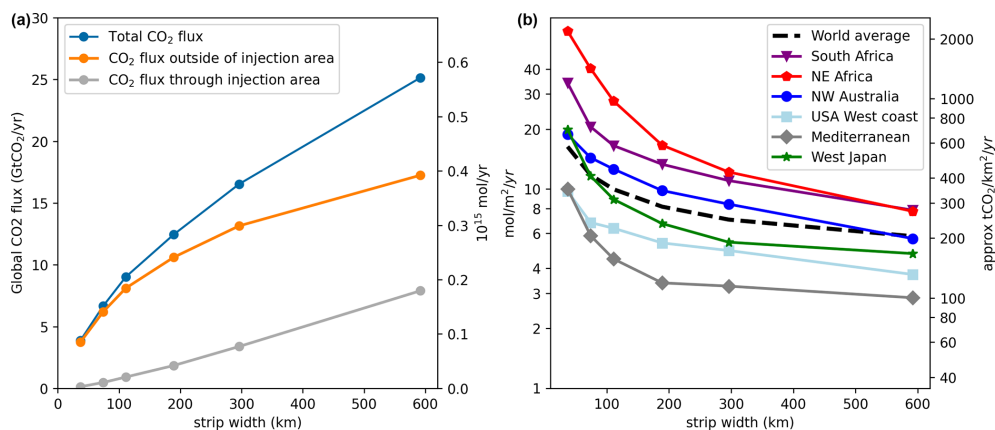
Figure 2. (a) Total CO_2 flux (Gt CO_2 yr^{-1}), subject to $\Delta pH_{tgt} = 0.1$, broken down into flux through the injection area and outside of the injection area. **(b)** Dependence of the averaged injection flux (mol m^{-2} yr^{-1}) on the width of the coastal injection strip for different coastal regions and strip widths. The black dashed line averages all coastal regions.

regional details are included in the Supplement in Fig. S4. Widening strips allows more alkalinity to be added overall. However, saturation of near-coast areas occurs in most regions (especially evident in Northwest Australia). The largest injection flux is often found directly at the strip boundary, owing to easy diffusion out to open sea. However, it is not always the case that the highest injection flux occurs at the strip edge, as seen in the Japan and East Africa examples. These findings illustrate the highly non-local nature of the injection capacity.

In general we find that the sensitivity of pH and Ω_{Arag} at any given grid point is highly dependent on the surrounding pattern of injection. We conducted two additional experiments in which rather than a contiguous strip, injection oc-

curred at discrete points placed either 200 or 400 km apart. At 200 km apart we observed much higher injection fluxes in each injection patch, but the total global injection flux barely changed (Fig. 4). Placing injection patches 400 km apart instead of 200 km apart did not further increase the sustainable flux in each injection patch, and reduced the overall injection capacity by 25 %. This suggests that at 200 km there is still significant cross-correlation between neighboring patches, which is apparent when looking at the pH changes observed: the pH impact bleeds into neighboring patches (Fig. 4b). At 400 km apart, however, there is much less interference between adjacent patches and the injection limits are simply dominated by local current patterns (Fig. 4c). These observations are consistent with prior work (Jones et al., 2012) which
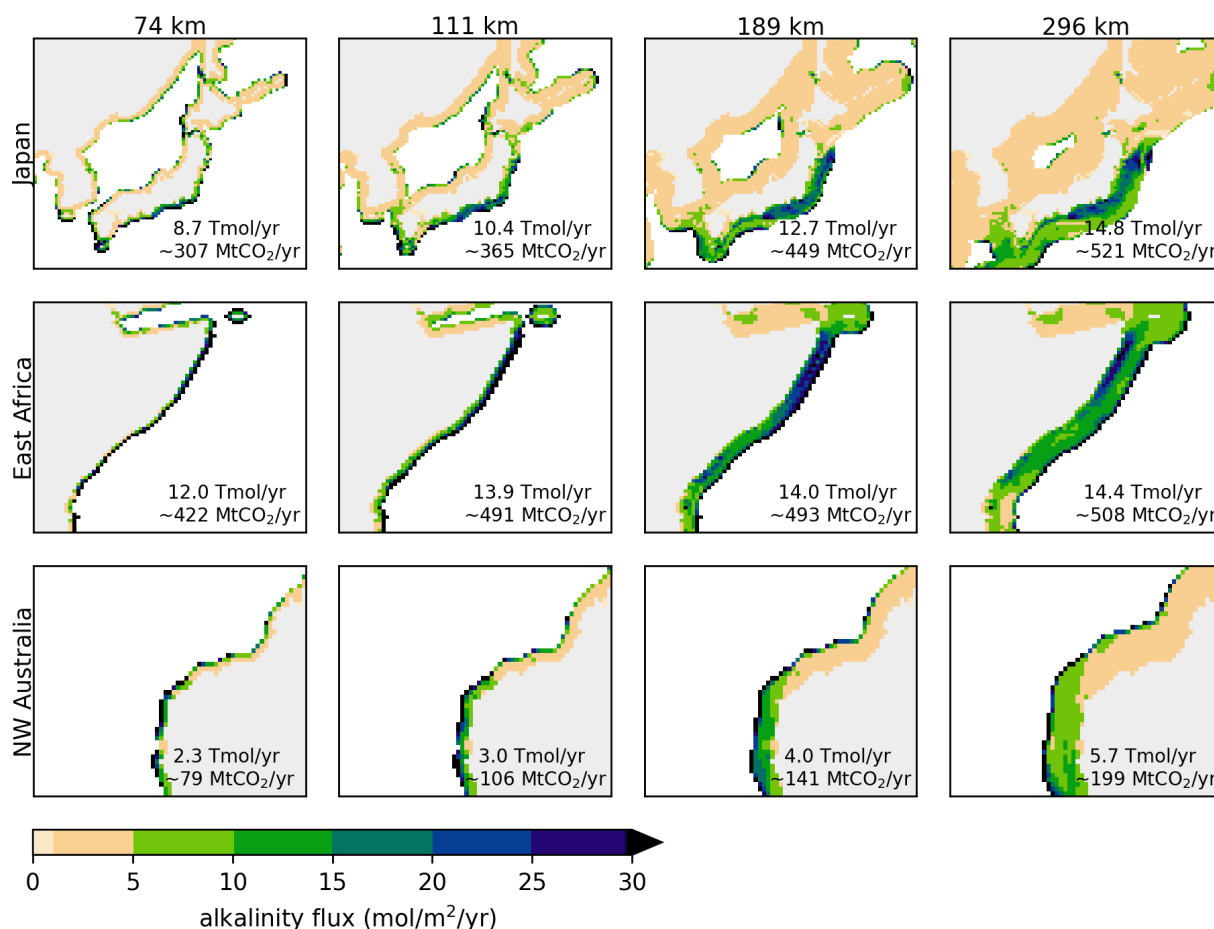
Figure 3. Injection flux ($\mathrm{mol\,m^{-2}\,yr^{-1}}$) shown for different strip widths in 3 different regions (from top to bottom: Japan, East Africa and Northwest Australia). The inset text indicates the total alkalinity added per year in the shown area.

found a global median pCO$_2$ autocorrelation length of about 400 km. Thus in order to maximize any particular coastline's injection potential, injection areas should be placed at most 200–400 km apart; however, the exact optima will depend on the local current patterns. The location of ports, infrastructure, access to electricity and/or alkaline minerals will dictate the choice of locations. The correlation between neighboring injection locations has ramifications for the planning, monitoring and governance of different OAE projects, as they will affect each other in downstream coastal areas. For monitoring and verification purposes it will be impossible to disambiguate CO$_2$ drawdown caused by different OAE projects by measurement alone. Any plans to add alkalinity to the ocean will need to be simulated specifically, ideally with regionally optimized models, and take into account already occurring OAE projects nearby.

3.2 CO$_2$ uptake time scales

To measure localized CO$_2$ uptake time scales, we conducted a total of 17 pulse injections (as described in the methods section), placed near all major coastlines. We generally chose

locations previously determined as areas of high alkalinity tolerance. Firstly, we observed a very large variety of CO$_2$ uptake time scales (Fig. 5) both in the short term (after 1 year) and in the medium term (after 10 years). After 1 year the molar uptake fraction $\eta_{\mathrm{CO_2}} = \Delta\mathrm{DIC}/\Delta\mathrm{Alk}$ varied between 0.2 and 0.85 and after 10 years most locations resulted in an uptake fraction of 0.65–0.80 consistent with previous work (Tyka et al., 2022; Burt et al., 2021).

A typical behavior is observed, for example, when releasing alkalinity at the northern coast of Brazil (Fig. 6a). Here the alkalinity remains long enough at the surface to realize its full CO$_2$ uptake potential within 2–3 years. A number of other tested locations follow this general pattern and are efficient for OAE deployment (Fig. 5a). Here the equilibration follows roughly a single exponential relaxation.

Another set of locations appear to lose a significant amount of alkalinity to deeper layers before atmospheric equilibration is achieved (Fig. 5b, c). For example, injection off the coast of Japan resulted in slow initial uptake as a portion of the alkalinity is quickly subducted (Fig. 6b). However, in the following decade remixing with surface waters gradu-
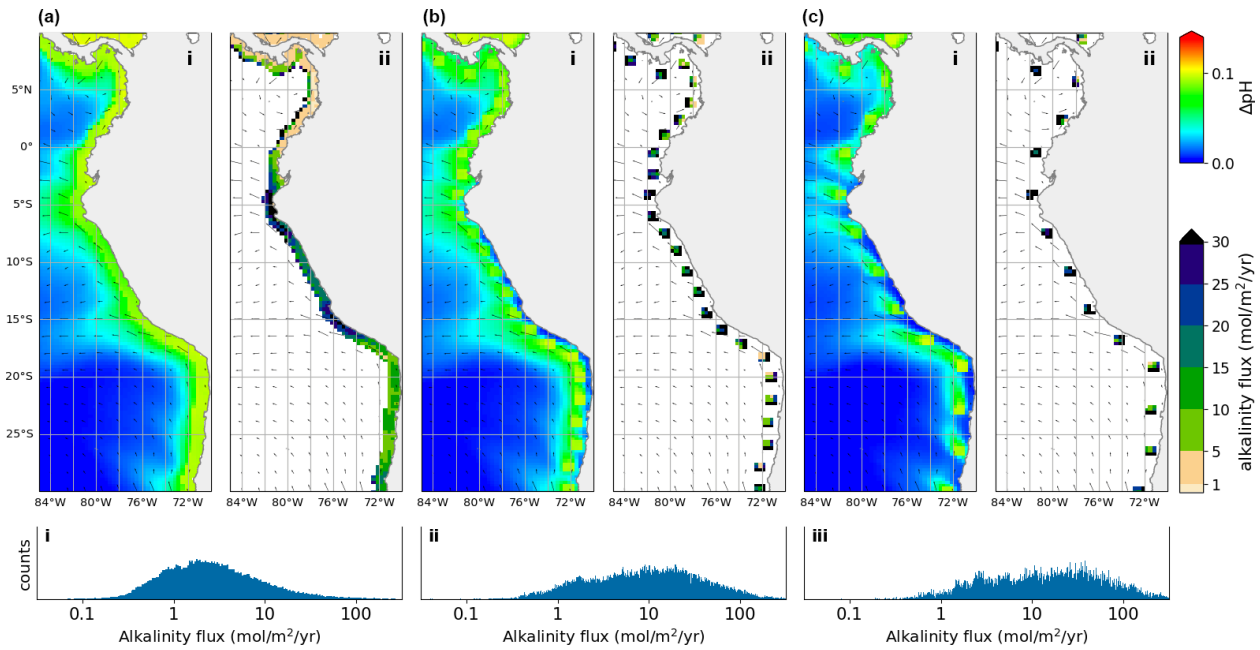
Figure 4. Alkalinity enhancement in three different patterns, exemplified at the west coast of South America: **(a)** Injection in a contiguous strip. **(b)** Injection in 200 km separated patches. **(c)** Injection in 400 km separated patches. The total globally area-integrated OAE rate for the three injection patterns was **(a)** 336 Tmol yr^{-1}, **(b)** 312 Tmol yr^{-1} and **(c)** 233 Tmol yr^{-1}, respectively. The sub panels show **(i)** time averaged pH change, **(ii)** alkalinity flux, **(iii)** distribution of alkalinity flux (globally).
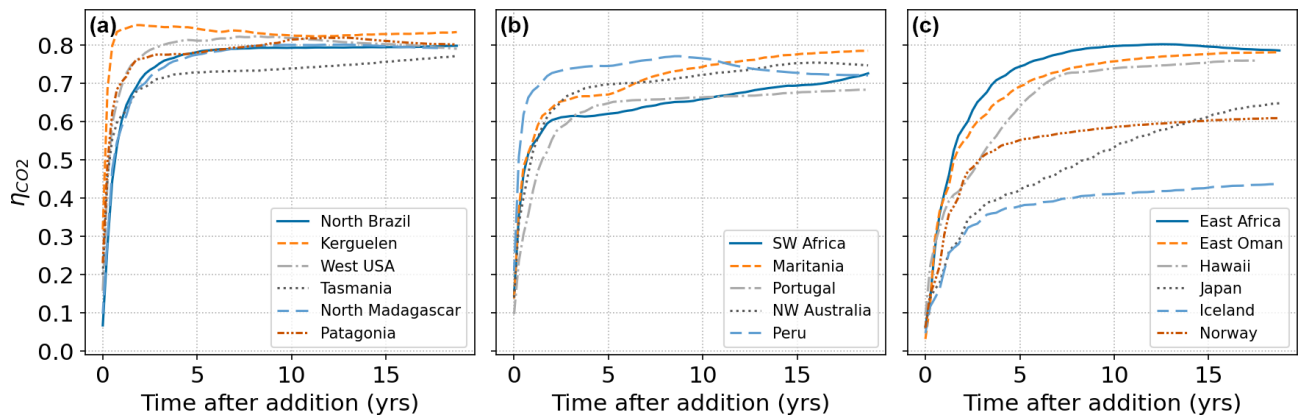
Figure 5. CO$_2$ uptake relative to alkalinity addition (molar ratio $\eta_{CO_2} = \Delta DIC/\Delta Alk$) following pulse additions at 17 different locations. **(a)** Locations which equilibrate fast and reach close to the theoretical maximum of CO$_2$ uptake (~ 0.8). **(b)** Locations which equilibrate fast but reach a lower plateau of relative CO$_2$ absorption (0.6–0.8) with slow further progression. **(c)** Locations with slow equilibration or significant loss of alkalinity to the deep. Note that in some cases despite the slower initial equilibration high uptake ratios can be eventually achieved.

ally returns this alkalinity back towards the surface resulting in slow but steady CO$_2$ uptake (Fig. 6b). Other examples of this delayed CO$_2$ equilibration are shown in Fig. 5b. These locations exhibit a short mixed layer residence time and have a poor equilibration efficiency (Jones et al., 2014), but equilibration is eventually achieved in the following decades. Changes in surface pCO$_2$ and alkalinity will also potentially affect biological CO$_2$ uptake and calcification rates; however, these dependencies are not captured by the carbonate model

used here (Dutkiewicz et al., 2005) and will need to be examined by future studies.

Finally, some extreme examples of poor long-term equilibration efficiency are found in areas of deep water formation, such as the northern Atlantic. Here a CO$_2$ uptake ratio of just over 0.4 is achieved and even after 20 years very little further progress is made (Fig. 6c). Around half of the added alkalinity is subducted very deep and will likely remain out of contact with the atmosphere until the global overturning
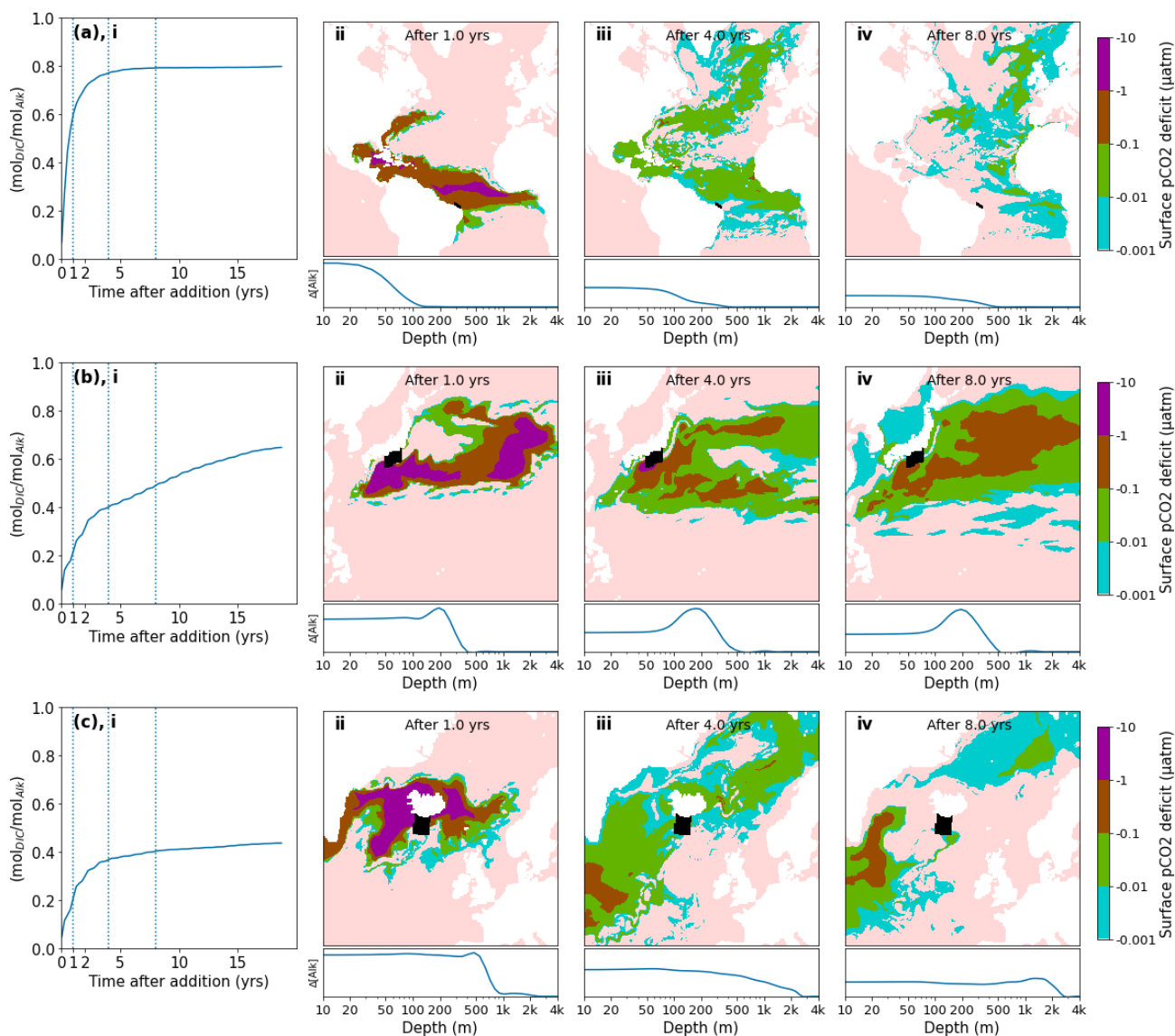
Figure 6. Pulse additions of alkalinity in 3 representative locations: **(a)** Brazil, **(b)** Japan, **(c)** Iceland. **(i)** Excess quantity of CO_2 absorbed (relative to the reference simulation) over time following a 1 month pulse injection at various near coast locations, expressed as a molar fraction of the amount of alkalinity added (η_{CO_2}). A significant variation of uptake time scales is observed, depending on the speed at which excess alkalinity is removed from surface layers, both in the short term and in the long term. **(ii–iv)** Spatial detail of surface pCO_2 deficit and depth residence of excess alkalinity for the same 3 locations shown in **(i)**. The initial injection location is indicated by a black area. The surface pCO_2 deficit is plotted over time (note the log scale of the color map), indicating areas which are absorbing extra CO_2 (or emitting less CO_2) compared to the reference simulation. Below, the relative excess alkalinity is plotted against the depth of the water column (averaged over all lat/long grid points for each depth). Further locations are shown in detail in Fig. S5.

circulation returns these waters to the surface, on the time scale of many hundreds of years. We did not examine the dependence of the time of year (all of our pulses occurred in January) nor were we able to conduct an exhaustive set of locations as was done previously with a coarser global circulation model (Tyka et al., 2022). We note that for all cases the alkalinity-induced CO_2 deficit spreads over a very large area within 1 year and a significant fraction of the CO_2 uptake occurs after the deficits have diluted to the sub-µatm range.

This makes direct monitoring and verification of OAE extremely challenging and will likely need to rely on modeling and indirect experimental verification.

3.3 Alkalinity injection from ships

Other than potential ecological impacts on marine life intersecting the caustic release wake of an OAE ship, one concern is that a short Ω_{Arag} spike could induce precipitation of
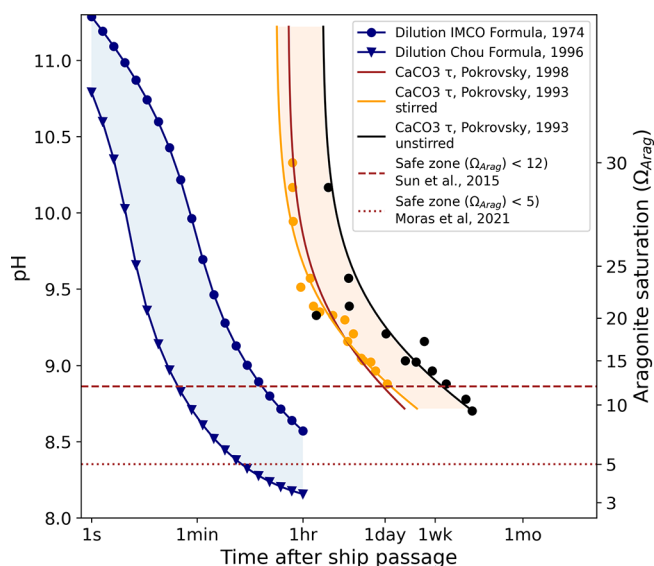
Figure 7. The expected time evolution of pH (left scale) and Ω_{Arag} (right scale) due to dilution for alkalinity injection into a ship wake. Here we assume a large tanker (275 m long, 50 m wide, traveling at $6\,m\,s^{-1}$) releasing 1.0 M NaOH at a rate of $5\,m^3\,s^{-1}$. Ships of this size have a capacity of 100–200 kt of cargo which would take 6–12 h to discharge. Two previously published dilution models are shown in blue with a large variance apparent. For comparison, the time scales of homogeneous nucleation are also shown (yellow, brown and black). The dashed and dotted lines indicate the estimated Ω limits for precipitation. Despite the substantial uncertainty in the existing models, dilution can proceed at least 1–2 orders of magnitude faster than precipitation is expected to occur.

$CaCO_3$ (Renforth, 2012). Once nucleated, the $CaCO_3$ particles could continue to grow, even when the pH has returned to normal ocean levels (≈ 8.1) because the ocean is supersaturated with respect to calcite ($\Omega_{Calc} \approx 2.5$–6) and aragonite ($\Omega_{Arag} \approx 1.5$–4) (Lauvset et al., 2016; Olsen et al., 2017). While the nucleation of $CaCO_3$ is strongly inhibited by the presence of magnesium in seawater (Sun et al., 2015; Pan et al., 2021), the growth of existing crystals may not be (Moras et al., 2022; Hartmann et al., 2022). Only once the $CaCO_3$ particle has reached a size and density that causes it to sink would it stop removing alkalinity from the surface ocean. Thus, depending on the number of particles nucleated, the alkalinity removed from the surface ocean can be larger than the alkalinity added (Moras et al., 2022; Hartmann et al., 2022; Fuhr et al., 2022).

As the immediate dilution dynamics of alkalinity injected into the wake of a ship are far below the resolution of the ECCO LLC270 global circulation model, we examine this process analytically, as described in the methods section. The relevant time scales are compared in Fig. 7. The predicted pH and Ω_{Arag} as a function of time are shown in blue, based on the dilution formulas given by IMCO (1975) and Chou (1996).

Also shown are the homogeneous nucleation times of $CaCO_3$ for comparison. Several studies (Pokrovsky, 1994, 1998) have measured the homogeneous nucleation of $CaCO_3$ in seawater at different saturation states down to $\Omega_{Arag} = 9$. Three of these models are plotted in shades of orange and black in Fig. 7. Theoretical studies (Sun et al., 2015) suggest that for Mg : Ca ratios of 5.2, as found in seawater, no nucleation of aragonite occurs at all below $\Omega_{Calc} = 18$ (equivalent to $\Omega_{Arag} \approx 12$), due to inhibition by magnesium. This is consistent with Morse and He (1993); however, time scales only up to a few hours were examined. Moras et al. (2022) suggested a safe limit of $\Omega_{Arag} = 5$ based on alkalinity addition using CaO. Figure 7 shows that ship-wake dilution proceeds at least one order of magnitude faster than the homogeneous nucleation time; thus, we can expect that $CaCO_3$ particles will not be induced to nucleate.

At the immediate injection site where the pH exceeds ~ 9.5–10.0, the temporary precipitation of $Mg(OH)_2$ is expected, which redissolves readily upon dilution (Pokrovsky and Savenko, 1995) and buffers the pH against further increase (not accounted for in Fig. 7). The temporary reduction in the Mg : Ca ratio could make $CaCO_3$ nucleation more favorable, but the time spent in this state (< 1 min) is likely still well below the required nucleation time.

3.4 Transport costs

Alkalinity prepared on land must be transported out to sea, which incurs costs. Having obtained maps of the sustainable rate of OAE in any given area, we can estimate the transport costs for each of our simulated scenarios as described in the methods section. Furthermore, the quantity of alkalinity per tonne depends on the molality of the material moved. For rock-based methods (Hangx and Spiers, 2009; Schuiling and de Boer, 2011; Renforth, 2012; Montserrat et al., 2017; Rigopoulos et al., 2018; Meysman and Montserrat, 2017), the molality of solid alkaline materials such as olivine is $\sim 25\,mol\,kg^{-1}$. For electrochemical alkalinity methods (House et al., 2007; Rau, 2009; Davies et al., 2018; Eisaman et al., 2018; de Lannoy et al., 2018; Digdaya et al., 2020) that produce alkaline liquids it will be closer to $1\,mol\,kg^{-1}$, depending on the industrial processes used and effort spent concentrating the alkaline solution. Figure 8 shows how the transportation costs are influenced by the total desired negative emissions (larger scale requires transport further offshore). For concentrated alkalinity (such as ground rocks) transport costs are not a major contributor to cost, consistent with prior work (Renforth, 2012). However, for dilute alkalinity, such as that obtained from electrochemical processes, transportation could become a significant contributor to the overall cost. A potential low-cost solution could be, for example, the near-coast precipitation (Thorsen et al., 2000; Davies et al., 2018; Sano et al., 2018) of $Mg(OH)_2$ with subsequent redissolution of the solid $Mg(OH)_2$ after transport out to sea. However, economic tradeoffs between the cost of
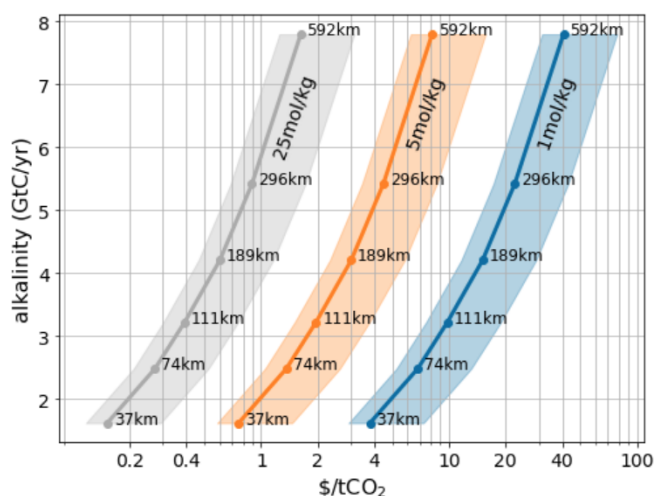
Figure 8. Total carbon uptake potential for a variable alkalinity addition strategy that results in a maximal pH change of 0.1 (see Fig. 1 for an example). Carbon uptake is estimated at $\eta_{CO_2} = 0.8$. The strip widths necessary are indicated for each point. Shading denotes the shipping cost uncertainty, which ranges from USD 0.0016 to 0.004 per tonne per kilometer (Renforth, 2012).

concentrating the alkalinity and the cost of transportation will need to be made.

4 Conclusions

In this paper we examined the suitability and effectiveness of near-coast regions of the ocean for alkalinity enhancement (OAE). We conducted a series of high resolution (0.3°) global circulation simulations in which alkalinity was added to coastal strips of varying width under the constraint of limited ΔpH or $\Delta\Omega_{Arag}$. We found that the resultant steady-state rate at which alkalinity can be added at any given location exhibits complex patterns and non-local dependencies which vary from region to region. The allowable injection rate is highly dependent on the surrounding injection pattern and varies over time, responding to external seasonal factors which are not always predictable. This makes it difficult to prevent occasional short spiking beyond the specified limit, thus potentially requiring that the limit is set conservatively in practice. These difficulties are also expected to arise in practice and have repercussions on how such OAE would be performed in reality and how it would be monitored, reported and verified (MRV). The non-local nature of the pH effect also likely requires different adjacent countries to coordinate their OAE efforts.

We found that even within the relatively conservative constraints set, most regional stretches of coastline are able to accommodate on the order of 10s to 100s of megatonnes of negative emissions, with areas with access to fast currents being able to accommodate more, such as East Africa or the

coast of Peru. Globally we conclude that near-coastal OAE has the potential to scale to a few gigatonnes of CO_2 drawdown, if the effort is spread over the majority of available coastlines. However, given that many other factors will determine suitable locations (such as availability of appropriate alkaline minerals, low-cost energy and geopolitical suitability) the global potential may be lower in practice. We also examined the cost of transport of alkalinity, which increases with global deployment size as the alkaline material needs to be spread over greater distances from the shore. For alkalinity schemes based on dry minerals the transport costs remain minor, but for electrochemical methods, which produce more dilute alkalinity, this may present limits to scaling.

We also examined the effectiveness and time scale of alkalinity enhancement on uptake of CO_2, through pulsed injections and subsequent tracking of surface water equilibration. Depending on the location, we find a complex set of equilibration kinetics. Most locations reach a plateau of 0.6–0.8 mol CO_2 per mol of alkalinity after 3–4 years, after which there is little further CO_2 uptake. The plateau efficiency depends on the amount of alkalinity lost to the deep ocean which will not equilibrate with the atmosphere until it returns to the surface, on the time scale of 100–500 years or more. The most ideal locations, reaching close to the theoretical maximum of ≈ 0.8, include north Madagascar, Brazil, Peru, and locations close to the Southern Ocean, such as Tasmania, Kerguelen and Patagonia, where the gas exchange appears to occur faster than the surface residence time. The variation of the achievable CO_2 drawdown per unit alkalinity on time scales relevant to the climate change crisis and the speed at which equilibration is reached poses further difficulty for verification of CDR credits.

Further study to determine these uptake efficiencies, at a finer location sample resolution and ideally with model ensembles, are needed for optimal placement of OAE deployments. While our results give an overall picture and are indicative of the complexity, more sophisticated biogeochemistry models (e.g., Carroll et al., 2022) and higher resolution regionally coupled biogeophysical models (e.g., Sein et al., 2015; Wang et al., 2022) will be essential for simulation and deployment of real-world OAE projects. It would also be interesting to examine how the CDR efficiency and OAE limits change in different future emission scenarios. At higher pCO_2 the ocean surface would be more acidic, and thus a larger OAE rate could be sustained without exceeding preindustrial surface pH. Increased stratification may increase surface residence times, thus decreasing the equilibration time. Furthermore, changes in biological activity, general circulation patterns and atmospheric dynamics further complicate the picture. Such effects and their interplay could potentially be studied in a full Earth system model under different emission scenarios.

References

Albright, R., Caldeira, L., Hosfelt, J., Kwiatkowski, L., Maclaren, J. K., Mason, B. M., Nebuchina, Y., Ninokawa, A., Pongratz, J., Ricke, K. L., Rivlin, T., Schneider, K., Sesboüé, M., Shamberger, K., Silverman, J., Wolfe, K., Zhu, K., and Caldeira, K.: Reversal of ocean acidification enhances net coral reef calcification, Nature, 531, 362–365, https://doi.org/10.1038/nature17155, 2016.

Archer, D., Eby, M., Brovkin, V., Ridgwell, A., Cao, L., Mikolajewicz, U., Caldeira, K., Matsumoto, K., Munhoven, G., Montenegro, A., and Tokos, K.: Atmospheric Lifetime of Fossil Fuel Carbon Dioxide, Annu. Rev. Earth Pl. Sc., 37, 117–134, https://doi.org/10.1146/annurev.earth.031208.100206, 2009.

Bach, L. T., Gill, S. J., Rickaby, R. E. M., Gore, S., and Renforth, P.: CO_2 Removal With Enhanced Weathering and Ocean Alkalinity Enhancement: Potential Risks and Co-benefits for Marine Pelagic Ecosystems, Frontiers in Climate, 1, 7, https://doi.org/10.3389/fclim.2019.00007, 2019.

Burt, D. J., Fröb, F., and Ilyina, T.: The Sensitivity of the Marine Carbonate System to Regional Ocean Alkalinity Enhancement, Frontiers in Climate, 3, 624075, https://doi.org/10.3389/fclim.2021.624075, 2021.

Byrne, C., Law, R., Hudson, P., Thain, J., and Fileman, T.: Measurements of the dispersion of liquid industrial waste discharged into the wake of a dumping vessel, Water Res., 22, 1577–1584, https://doi.org/10.1016/0043-1354(88)90171-6, 1988.

Carroll, D., Menemenlis, D., Adkins, J. F., Bowman, K. W., Brix, H., Dutkiewicz, S., Fenty, I., Gierach, M. M., Hill, C., Jahn, O., Landschützer, P., Lauderdale, J. M., Liu, J., Manizza, M., Naviaux, J. D., Rödenbeck, C., Schimel, D. S., Van der Stocken, T., and Zhang, H.: The ECCO-Darwin Data-Assimilative Global Ocean Biogeochemistry Model: Estimates of Seasonal to Multidecadal Surface Ocean pCO$_2$ and Air-Sea CO_2 Flux, J. Adv. Model. Earth Sy., 12, e2019MS001888, https://doi.org/10.1029/2019MS001888, 2020.

Carroll, D., Menemenlis, D., Dutkiewicz, S., Lauderdale, J. M., Adkins, J. F., Bowman, K. W., Brix, H., Fenty, I., Gierach, M. M., Hill, C., Jahn, O., Landschützer, P., Manizza, M., Mazloff, M. R., Miller, C. E., Schimel, D. S., Verdy, A., Whitt, D. B., and Zhang, H.: Attribution of Space-Time Variability in Global-Ocean Dissolved Inorganic Carbon, Global Biogeochem. Cy., 36, e2021GB007162, https://doi.org/10.1029/2021GB007162, 2022.

Chou, H.-T.: On the dilution of liquid waste in ships' wakes, J. Mar. Sci. Technol., 1, 149–154, https://doi.org/10.1007/BF02391175, 1996.

Davies, P. A., Yuan, Q., and de Richter, R.: Desalination as a negative emissions technology, Environ. Sci.-Wat. Res., 4, 839–850, https://doi.org/10.1039/C7EW00502D, 2018.

de Lannoy, C.-F., Eisaman, M. D., Jose, A., Karnitz, S. D., DeVaul, R. W., Hannun, K., and Rivest, J. L.: Indirect ocean capture of atmospheric CO_2: Part I. Prototype of a negative emissions technology, Int. J. Greenh. Gas Con., 70, 243–253, https://doi.org/10.1016/j.ijggc.2017.10.007, 2018.

Digdaya, I. A., Sullivan, I., Lin, M., Han, L., Cheng, W.-H., Atwater, H. A., and Xiang, C.: A direct coupled electrochemical system for capture and conversion of CO_2 from oceanwater, Nat. Commun., 11, 362–365, https://doi.org/10.1038/s41467-020-18232-y, 2020.

Doney, S. C., Fabry, V. J., Feely, R. A., and Kleypas, J. A.: Ocean Acidification: The Other CO_2 Problem, Annu. Rev. Mar. Sci., 1, 169–192, https://doi.org/10.1146/annurev.marine.010908.163834, 2009.

Dutkiewicz, S., Sokolov, A., Scott, J., and Stone, P.: A three-dimensional ocean-seaice-carbon cycle model and its coupling to a two dimensional atmospheric model: Uses in climate change studies. Report 122, MIT Joint Program on the Science and Policy of Global Change, http://mit.edu/globalchange/www/MITJPSPGC_Rpt122.pdf (last access: 20 April 2021), 2005.

Eisaman, M. D., Rivest, J. L., Karnitz, S. D., de Lannoy, C.-F., Jose, A., DeVaul, R. W., and Hannun, K.: Indirect ocean capture of atmospheric CO_2: Part II. Understanding the cost of negative emissions, Int. J. Greenh. Gas Con., 70, 254–261, https://doi.org/10.1016/j.ijggc.2018.02.020, 2018.

Fakhraee, M., Li, Z., Planavsky, N., and Reinhard, C.: Environmental impacts and carbon capture potential of ocean alkalinity enhancement, 11 April 2022, PREPRINT (Version 1),Research Square, https://doi.org/10.21203/rs.3.rs-1475007/v1, 2022.

Fassbender, A. J., Orr, J. C., and Dickson, A. G.: Technical note: Interpreting pH changes, Biogeosciences, 18, 1407–1415, https://doi.org/10.5194/bg-18-1407-2021, 2021.

Feng, E. Y., Keller, D. P., Koeve, W., and Oschlies, A.: Could artificial ocean alkalinization protect tropical coral ecosystems from ocean acidification?, Environ. Res. Lett., 11, 074008, https://doi.org/10.1088/1748-9326/11/7/074008, 2016.

Feng, E. Y., Koeve, W., Keller, D. P., and Oschlies, A.: Model-Based Assessment of the CO_2 Sequestration Potential of Coastal Ocean Alkalinization, Earth's Future, 5, 1252–1266, https://doi.org/10.1002/2017EF000659, 2017.

Ferderer, A., Chase, Z., Kennedy, F., Schulz, K. G., and Bach, L. T.: Assessing the influence of ocean alkalinity enhancement on a coastal phytoplankton community, Biogeosciences Discuss. [preprint], https://doi.org/10.5194/bg-2022-17, in review, 2022.

Fuhr, M., Geilert, S., Schmidt, M., Liebetrau, V., Vogt, C., Ledwig, B., and Wallmann, K.: Kinetics of Olivine Weathering in Seawater: An Experimental Study, Frontiers in Climate, 4, 831587, https://doi.org/10.3389/fclim.2022.831587, 2022.

Gernon, T. M., Hincks, T. K., Merdith, A. S., Rohling, E. J., Palmer, M. R., Foster, G. L., Bataille, C. P., and Müller, R. D.: Global chemical weathering dominated by continental arcs since the mid-Palaeozoic, Nat. Geosci., 14, 690–696, https://doi.org/10.1038/s41561-021-00806-0, 2021.

Goldberg, D. S., Takahashi, T., and Slagle, A. L.: Carbon dioxide sequestration in deep-sea basalt, P. Natl. Acad. Sci. USA, 105, 9920–9925, https://doi.org/10.1073/pnas.0804397105, 2008.

González, M. F. and Ilyina, T.: Impacts of artificial ocean alkalinization on the carbon cycle and climate in Earth system simulations, Geophys. Res. Lett., 43, 6493–6502, https://doi.org/10.1002/2016gl068576, 2016.

Guo, J. A., Strzepek, R., Willis, A., Ferderer, A., and Bach, L. T.: Investigating the effect of nickel concentration on phytoplankton growth to assess potential side-effects of ocean alkalinity enhancement, Biogeosciences, 19, 3683–3697, https://doi.org/10.5194/bg-19-3683-2022, 2022.

Hangx, S. J. and Spiers, C. J.: Coastal spreading of olivine to control atmospheric CO_2 concentrations: A critical analysis of viability, Int. J. Greenh. Gas Con., 3, 757–767, https://doi.org/10.1016/j.ijggc.2009.07.001, 2009.

Hartmann, J., Suitner, N., Lim, C., Schneider, J., Marín-Samper, L., Arístegui, J., Renforth, P., Taucher, J., and Riebesell, U.: Stability of alkalinity in Ocean Alkalinity Enhancement (OAE) approaches – consequences for durability of CO_2 storage, Biogeosciences Discuss. [preprint], https://doi.org/10.5194/bg-2022-126, in review, 2022.

He, J. and Tyka, M. D.: Limits and equilibration dynamics of near-coast alkalinity enhancement (Version 0), Zenodo [code and data set], https://doi.org/10.5281/zenodo.7460358, 2022.

House, K. Z., House, C. H., Schrag, D. P., and Aziz, M. J.: Electrochemical Acceleration of Chemical Weathering as an Energetically Feasible Approach to Mitigating Anthropogenic Climate Change, Environ. Sci. Technol., 41, 8464–8470, https://doi.org/10.1021/es0701816, 2007.

Humphreys, M. P., Gregor, L., Pierrot, D., van Heuven, S. M. A. C., Lewis, E. R., and Wallace, D. W. R.: PyCO2SYS: marine carbonate system calculations in Python, Zenodo [code], https://doi.org/10.5281/ZENODO.3744275, 2020.

Ilyina, T., Wolf-Gladrow, D., Munhoven, G., and Heinze, C.: Assessing the potential of calcium-based artificial ocean alkalinization to mitigate rising atmospheric CO_2 and ocean acidification, Geophys. Res. Lett., 40, 5909–5914, 2013.

IMCO: Procedures and arrangements for the discharge of noxious liquid substances. Method for calculation of dilution capacity in the ship's wake, IMCO document MEPC III-7, 27 May 1975, 1975.

Jones, D. C., Ito, T., Takano, Y., and Hsu, W.-C.: Spatial and seasonal variability of the air-sea equilibration timescale of carbon dioxide, Global Biogeochem. Cy., 28, 1163–1178, https://doi.org/10.1002/2014GB004813, 2014.

Jones, S. D., Le Quéré, C., and Rödenbeck, C.: Autocorrelation characteristics of surface ocean pCO_2 and air-sea CO_2 fluxes, Global Biogeochem. Cy., 26, GB2042, https://doi.org/10.1029/2010GB004017, 2012.

Keller, D. P., Feng, E. Y., and Oschlies, A.: Potential climate engineering effectiveness and side effects during a high carbon dioxide-emission scenario, Nat. Commun., 5, 3304, https://doi.org/10.1038/ncomms4304, 2014.

Keller, D. P., Lenton, A., Littleton, E. W., Oschlies, A., Scott, V., and Vaughan, N. E.: The Effects of Carbon Dioxide Removal on the Carbon Cycle, Current Climate Change Reports, 4, 250–265, https://doi.org/10.1007/s40641-018-0104-3, 2018.

Kheshgi, H. S.: Sequestering atmospheric carbon dioxide by increasing ocean alkalinity, Energy, 20, 915–922, https://doi.org/10.1016/0360-5442(95)00035-F, 1995.

Köhler, P., Abrams, J. F., Völker, C., Hauck, J., and Wolf-Gladrow, D. A.: Geoengineering impact of open ocean dissolution of olivine on atmospheric CO_2, surface ocean pH and marine biology, Environ. Res. Lett., 8, 014009, https://doi.org/10.1088/1748-9326/8/1/014009, 2013.

Lauvset, S. K., Key, R. M., Olsen, A., van Heuven, S., Velo, A., Lin, X., Schirnick, C., Kozyr, A., Tanhua, T., Hoppema, M., Jutterström, S., Steinfeldt, R., Jeansson, E., Ishii, M., Perez, F. F., Suzuki, T., and Watelet, S.: A new global interior ocean mapped climatology: the $1° \times 1°$ GLODAP version 2, Earth Syst. Sci. Data, 8, 325–340, https://doi.org/10.5194/essd-8-325-2016, 2016.

Lewis, E. R. and Wallace, D. W. R.: Program Developed for CO_2 System Calculations, ESS-Dive [data set], https://doi.org/10.15485/1464255, 1998.

Lewis, R.: The dilution of waste in the wake of a ship, Water Res., 19, 941–945, https://doi.org/10.1016/0043-1354(85)90360-4, 1985.

Lewis, R. E. and Riddle, A. M.: Sea disposal: Modelling studies of waste field dilution, Mar. Pollut. Bull., 20, 124–129, https://doi.org/10.1016/0025-326x(88)90817-x, 1989.

Li, J. and Hitch, M.: Ultra-fine grinding and mechanical activation of mine waste rock using a high-speed stirred mill for mineral carbonation, Int. J. Min. Met. Mater., 22, 1005–1016, https://doi.org/10.1007/s12613-015-1162-3, 2015.

Marshall, J., Adcroft, A., Hill, C., Perelman, L., and Heisey, C.: A finite-volume, incompressible Navier Stokes model for studies of the ocean on parallel computers, J. Geophys. Res.-Oceans, 102, 5753–5766, https://doi.org/10.1029/96JC02775, 1997.

IPCC: Summary for Policymakers. In: Climate Change 2021: The Physical Science Basis, Contribution of Working Group I to the Sixth Assessment Report of the Intergovernmental Panel on Climate Change, edited by: Masson-Delmotte, V., Zhai, P., Pirani, A., Connors, S. L., Péan, C., Berger, S., Caud, N., Chen, Y., Goldfarb, L., Gomis, M. I., Huang, M., Leitzell, K., Lonnoy, E., Matthews, J. B. R., Maycock, T. K., Waterfield, T., Yelekçi, O., Yu, R., and Zhou, B.: Cambridge University Press, Cambridge, United Kingdom and New York, NY, USA, 3–32, https://doi.org/10.1017/9781009157896.001, 2021.

Matter, J. M., Broecker, W., Stute, M., Gislason, S., Oelkers, E., Stefánsson, A., Wolff-Boenisch, D., Gunnlaugsson, E., Axelsson, G., and Björnsson, G.: Permanent Carbon Dioxide Storage into Basalt: The CarbFix Pilot Project, Iceland, Enrgy. Proced., 1, 3641–3646, https://doi.org/10.1016/j.egypro.2009.02.160, 2009.

McGrail, B. P., Schaef, H. T., Ho, A. M., Chien, Y.-J., Dooley, J. J., and Davidson, C. L.: Potential for carbon dioxide sequestration in flood basalts, J. Geophys. Res., 111, B12201, https://doi.org/10.1029/2005jb004169, 2006.

IPCC: IPCC Special Report on Carbon Dioxide Capture and Storage, Prepared by Working Group III of the Intergovernmental Panel on Climate Change, edited by: Metz, B., Davidson, O., de Coninck, H. C., Loos, M., and Meyer, L. A., Cambridge University Press, Cambridge, United Kingdom and New York, NY, USA, 442 pp., https://www.ipcc.ch/report/carbon-dioxide-capture-and-storage/ (last access: 1 June 2022), 2005.

Meysman, F. J. R. and Montserrat, F.: Negative CO_2 emissions via enhanced silicate weathering in coastal environments, Biol. Lett., 13, 20160905, https://doi.org/10.1098/rsbl.2016.0905, 2017.

Middelburg, J. J., Soetaert, K., and Hagens, M.: Ocean Alkalinity, Buffering and Biogeochemical Processes, Rev. Geophys., 58, e2019RG000681, https://doi.org/10.1029/2019rg000681, 2020.

Montserrat, F., Renforth, P., Hartmann, J., Leermakers, M., Knops, P., and Meysman, F. J. R.: Olivine Dissolution in Seawater: Implications for CO_2 Sequestration through Enhanced Weathering in Coastal Environments, Environ. Sci. Technol., 51, 3960–3972, https://doi.org/10.1021/acs.est.6b05942, 2017.

Moras, C. A., Bach, L. T., Cyronak, T., Joannes-Boyau, R., and Schulz, K. G.: Ocean alkalinity enhancement – avoiding runaway $CaCO_3$ precipitation during quick and hydrated lime dissolution, Biogeosciences, 19, 3537–3557, https://doi.org/10.5194/bg-19-3537-2022, 2022.

Morse, J. W. and He, S.: Influences of T, S and PCO_2 on the pseudo-homogeneous precipitation of $CaCO_3$ from seawater: implications for whiting formation, Mar. Chem., 41, 291–297, https://doi.org/10.1016/0304-4203(93)90261-L, 1993.

Olsen, A., Key, R. M., Lauvset, S. K., Kozyr, A., Tanhua, T., Hoppema, M., Ishii, M., Jeansson, E., Van Heuven, S. M. A. C., Jutterström, S., Schirnick, C., Steinfeldt, R., Suzuki, T., Lin, X., Velo, A., and Pérez, F. F.: Global Ocean Data Analysis Project, Version 2 (GLODAPv2) (NCEI Accession 0162565), NOAA [data set], https://doi.org/10.7289/V5KW5D97, 2017.

Pan, Y., Li, Y., Ma, Q., He, H., Wang, S., Sun, Z., Cai, W.-J., Dong, B., Di, Y., Fu, W., and Chen, C.-T. A.: The role of Mg_{2+} in inhibiting $CaCO_3$ precipitation from seawater, Mar. Chem., 237, 104036, 2021.

Penman, D. E., Caves Rugenstein, J. K., Ibarra, D. E., and Winnick, M. J.: Silicate weathering as a feedback and forcing in Earth's climate and carbon cycle, Earth-Sci. Rev., 209, 103298, https://doi.org/10.1016/j.earscirev.2020.103298, 2020.

Pokrovsky, O.: Precipitation of calcium and magnesium carbonates from homogeneous supersaturated solutions, J. Cryst. Growth, 186, 233–239, https://doi.org/10.1016/S0022-0248(97)00462-4, 1998.

Pokrovsky, O. and Savenko, V.: The role of magnesium at homogeneous precipitation of calcium carbonate from seawater, Oceanology, 34, 493–497, 1995.

Pokrovsky, O. S.: Kinetics of $CaCO_3$ Homogeneous Precipitation in Seawater, Mineral. Mag., 58A, 738–739, https://doi.org/10.1180/minmag.1994.58a.2.121, 1994.

Rau, G. H.: Electrochemical CO_2 capture and storage with hydrogen generation, Enrgy. Proced., 1, 823–828, https://doi.org/10.1016/j.egypro.2009.01.109, 2009.

Renforth, P.: The potential of enhanced weathering in the UK, Int. J. Greenh. Gas Con., 10, 229–243, https://doi.org/10.1016/j.ijggc.2012.06.011, 2012.

Renforth, P. and Henderson, G.: Assessing ocean alkalinity for carbon sequestration, Rev. Geophys., 55, 636–674, https://doi.org/10.1002/2016rg000533, 2017.

Riebesell, U. and Tortell, P. D.: Effects of Ocean Acidification on Pelagic Organisms and Ecosystems, in: Ocean Acidification, Oxford University Press, https://doi.org/10.1093/oso/9780199591091.003.0011, 2011.

Rigopoulos, I., Harrison, A. L., Delimitis, A., Ioannou, I., Efstathiou, A. M., Kyratsi, T., and Oelkers, E. H.: Carbon sequestration via enhanced weathering of peridotites and basalts in seawater, Appl. Geochem., 91, 197–207, https://doi.org/10.1016/j.apgeochem.2017.11.001, 2018.

Rogelj, J., Popp, A., Calvin, K. V., Luderer, G., Emmerling, J., Gernaat, D., Fujimori, S., Strefler, J., Hasegawa, T., Marangoni, G., Krey, V., Kriegler, E., Riahi, K., van Vuuren, D. P., Doelman, J., Drouet, L., Edmonds, J., Fricko, O., Harmsen, M., Havlík, P., Humpenöder, F., Stehfest, E., and Tavoni, M.: Scenarios towards limiting global mean temperature increase below 1.5 °C, Nat. Clim. Change, 8, 325–332, https://doi.org/10.1038/s41558-018-0091-3, 2018.

Sano, Y., Hao, Y., and Kuwahara, F.: Development of an electrolysis based system to continuously recover magnesium from seawater, Heliyon, 4, e00923, https://doi.org/10.1016/j.heliyon.2018.e00923, 2018.

Sarmiento, J. L. and Gruber, N.: Ocean biogeochemical dynamics, Princeton University Press, Princeton, oCLC: ocm60651167, ISBN: 9780691017075, 2006.

Schuiling, R. D. and de Boer, P. L.: Rolling stones; fast weathering of olivine in shallow seas for cost-effective CO_2 capture and mitigation of global warming and ocean acidification, Earth Syst. Dynam. Discuss., 2, 551–568, https://doi.org/10.5194/esdd-2-551-2011, 2011.

Sein, D. V., Mikolajewicz, U., Gröger, M., Fast, I., Cabos, W., Pinto, J. G., Hagemann, S., Semmler, T., Izquierdo, A., and Jacob, D.: Regionally coupled atmosphere-ocean-sea ice-marine biogeochemistry model ROM: 1. Description and validation, J. Adv. Model. Earth Sy., 7, 268–304, https://doi.org/10.1002/2014MS000357, 2015.

Subhas, A. V., Marx, L., Reynolds, S., Flohr, A., Mawji, E. W., Brown, P. J., and Cael, B. B.: Microbial ecosystem responses to alkalinity enhancement in the North Atlantic Subtropical Gyre, Frontiers in Climate, 4, https://doi.org/10.3389/fclim.2022.784997, 2022.

Sun, W., Jayaraman, S., Chen, W., Persson, K. A., and Ceder, G.: Nucleation of metastable aragonite $CaCO_3$ in seawater, P. Natl. Acad. Sci. USA, 112, 3199–3204, https://doi.org/10.1073/pnas.1423898112, 2015.

Thorsen, T. G., Hagen, R. I., Wærnes, O., and Langseth, B.: Method for production of magnesium hydroxide from sea

water, https://patentscope.wipo.int/search/en/detail.jsf?docId=WO2000029326 (last access: 1 June 2022), 2000.

Tyka, M. D., Van Arsdale, C., and Platt, J. C.: CO_2 capture by pumping surface acidity to the deep ocean, Energy Environ. Sci., 15, 786–798, https://doi.org/10.1039/D1EE01532J, 2022.

van Sebille, E., Griffies, S. M., Abernathey, R., Adams, T. P., Berloff, P., Biastoch, A., Blanke, B., Chassignet, E. P., Cheng, Y., Cotter, C. J., Deleersnijder, E., Döös, K., Drake, H. F., Drijfhout, S., Gary, S. F., Heemink, A. W., Kjellsson, J., Koszalka, I. M., Lange, M., Lique, C., MacGilchrist, G. A., Marsh, R., Mayorga Adame, C. G., McAdam, R., Nencioli, F., Paris, C. B., Piggott, M. D., Polton, J. A., Rühs, S., Shah, S. H., Thomas, M. D., Wang, J., Wolfram, P. J., Zanna, L., and Zika, J. D.: Lagrangian ocean analysis: Fundamentals and practices, Ocean Model., 121, 49–75, https://doi.org/10.1016/j.ocemod.2017.11.008, 2018.

Wang, H., Pilcher, D. J., Eisaman, M. D., and Carter, B. R.: Simulated impact of ocean alkalinity enhancement on atmospheric CO_2 removal in the Bering Sea, AGU Earth's Future, in press, https://doi.org/10.1029/2022EF002816, 2022.

Wanninkhof, R.: Relationship between wind speed and gas exchange over the ocean, J. Geophys. Res.-Oceans, 97, 7373–7382, https://doi.org/10.1029/92JC00188, 1992.

Wunsch, C. and Heimbach, P.: Chapter 21 – Dynamically and Kinematically Consistent Global Ocean Circulation and Ice State Estimates, in: Ocean Circulation and Climate, edited by: Siedler, G., Griffies, S. M., Gould, J., and Church, J. A., Vol. 103 of International Geophysics, 553–579, Academic Press, https://doi.org/10.1016/B978-0-12-391851-2.00021-0, 2013.

Wunsch, C., Heimbach, P., Ponte, R. M., Fukumori, I., and The ECCO-GODAE Consortium Members: The global general circulation of the ocean estimated by the ECCO-Consortium, Oceanography, 22, 88–103, https://doi.org/10.5670/oceanog.2009.41, 2009.

Zeebe, R. E. and Wolf-Gladrow, D. A.: CO_2 in seawater: Equilibrium, kinetics, isotopes: Volume 65, Elsevier Oceanography Series, Elsevier Science, London, UK, 2001.

Zhang, H., Menemenlis, D., and Fenty, I.: ECCO LLC270 Ocean-Ice State Estimate, https://dspace.mit.edu/handle/1721.1/119821 (last access: June 2022), 2018.